This is the accepted manuscript made available via CHORUS. The article has been published as:

Tip- and Plasmon-Enhanced Infrared Nanoscopy for Ultrasensitive Molecular Characterizations

Y. Luan, L. McDermott, F. Hu, and Z. Fei

Phys. Rev. Applied **13**, 034020 — Published 6 March 2020

DOI: 10.1103/PhysRevApplied.13.034020

Tip- and plasmon-enhanced infrared nanoscopy for ultrasensitive molecular characterizations

Y. Luan[1,2], L. McDermott[1], F. Hu[1,2], Z. Fei[1,2]*

[1]Department of Physics and Astronomy, Iowa State University, Ames, Iowa 50011, USA
[2]Ames Laboratory, U.S. Department of Energy, Iowa State University, Ames, Iowa 50011, USA

*Correspondence to: (Z.F.) zfei@iastate.edu.

ABSTRACT: We propose a novel method for ultra-sensitive infrared (IR) vibrational spectroscopy of molecules with nanoscale footprints by combining the tip enhancement of the scattering-type scanning near-field optical microscope (s-SNOM) and the plasmon enhancement of the breathing-mode (BM) plasmon resonances of graphene nanodisks (GNDs). To demonstrate that, we developed a quantitative model that is capable of computing accurately the s-SNOM signals of nanoscale samples. With our modeling, we show that the s-SNOM tip can effectively excite gate-tunable BM plasmonic resonances in GNDs with strong field enhancement and sensitive dependence on the size of GND. Moreover, we demonstrate that the intense electric field of tip-excited plasmonic BMs can strongly enhance the IR vibrational modes of molecules. As a result, IR vibrational signatures of individual molecular particles with sizes down to 1-2 nm can be readily observable by s-SNOM. Our study sheds light on future ultra-sensitive IR biosensing that takes advantage of both the tip and plasmon enhancement.

I. INTRODUCTION

Graphene plasmon polaritons are collective oscillations of Dirac fermions in graphene covering a broad spectral range from terahertz to infrared [1-7]. With both imaging and spectroscopy techniques [8-11], graphene plasmons have been extensively studied in recent years. Many superior characteristics have been discovered, such as electrical tunability [8-14], strong confinement [8-17], long lifetime [17,18], and high environmental sensitivity [17-19]. These unique properties lead to many technological innovations, among which plasmon-enhanced infrared spectroscopy (PEIS) is possibly the most promising one. Indeed, recent experimental studies demonstrated that graphene plasmon resonances can enhance the infrared (IR) vibrational modes of molecules or polymers [20-23]. In nearly all these studies, dipole-mode (DM) plasmon resonances of graphene nanostructures (GNS) were excited directly by far-field IR beams. Despite the success of PEIS demonstrated with GNS, the sensitivity is still too low to probe individual molecules or bio-particles, which is partly due to the diffraction-limited IR beam with a large beam size, and partly due to the relatively weak field enhancement of the DM plasmon resonances.

In order to increase the sensitivity for nanoscale IR characterizations of small molecules, stronger field enhancement and higher spatial resolution are necessary. For that purpose, we propose to take advantage of the breathing-mode (BM) plasmonic resonances [24-26] in graphene nanodisks (GNDs) that could induce even stronger field enhancement due to the circular symmetry. Unlike DM plasmon resonances, the plasmonic BMs have zero net polarization, so they are considered dark modes that cannot be excited directly by far-field optical beams [24]. To excite and probe these BMs, the scattering-type scanning near-field optical microscope (s-SNOM) [Fig. 1(a)] has been proven to be an effective tool [25]. When illuminated by a *p*-polarized laser, the sharp metallic s-SNOM tip acts as a nano-antenna that is perfect for exciting the circular-symmetric BMs in GNDs [Fig. 1(b)]. Moreover, the tip can further enhance the plasmon field due to the so-called "lightning-rod effect". As discussed below, the two-fold enhancement by both the tip and BM plasmons is the key to the ultra-high sensitivity of the proposed method here. Beside mode excitation and field enhancement, the s-SNOM tip also plays the role of plasmon field detection. Indeed, the radiation signal from the polarized s-SNOM tip collected by the detector offers an accurate measurement of the plasmon field right underneath the tip. Such a capability of tip excitation & detection of s-SNOM has been demonstrated in the studies of graphene plasmons [9-11] and other polaritonic modes in two-dimensional (2D) materials [27-36]. Furthermore, s-SNOM enables

nanoscale Fourier-transform IR spectroscopy (nano-FTIR) when coupled with a broadband IR laser, which is suitable for vibrational mode fingerprinting of nanoscale materials and biomolecules [37-40].

In this paper, we demonstrate with quantitative modeling that s-SNOM, when coupled with BM plasmon resonances of GNDs, is perfect for applications in ultra-sensitive PEIS. In the following sections, we will first introduce our quantitative s-SNOM model with an elongated tip shape, which is essential for accurately modeling the s-SNOM signals. We will then discuss the general characteristics of the tip-excited BM plasmons of GNDs with modeled nano-IR spectra and plasmon field patterns. Finally, we will demonstrate the ultra-high sensitivity of s-SNOM to vibrational modes of molecules due to the field enhancement by both the s-SNOM tip and the BM plasmon resonances.

II. RESULTS AND DISCUSSION

A. Quantitative s-SNOM model for nanoscale samples.

To model quantitatively the s-SNOM signals, we construct a numerical model based on the finite-element commercial solver Comsol Multiphysics. Note that there were several earlier works about quantitative models of s-SNOM [41-44], which typically assume infinite lateral sizes of samples for simplicity in computation. As discussed below, the Comsol-based s-SNOM model introduced here can be conveniently tailored for nanoscale samples with small dimensions. Depending on the symmetry of the samples in consideration, we choose either 2D axisymmetric or 3D Comsol models. The former is more efficient in computation and is more suitable for the modeling of BM plasmons of GNDs, and the latter can in principle be used to model sample structures with arbitrary geometries. The results with both models are consistent with each other. The results shown in this work are mainly obtained with the 2D axisymmetric model. Typical computation time for one complete spectrum with this model is only about 1 hour or less when using a common desktop workstation.

As illustrated in Fig. 1(a), the s-SNOM tip is modeled as the conducting spheroid with a length of L and a radius of curvature at the tip apex of a, where a is set to be about 25 nm according to the manufacturer and L is set to be 1200 nm to best fit the s-SNOM data of standard reference materials (SiO_2 and graphene, see Supplemental Material [45]). With the 2D axisymmetric model, we evaluate numerically the total radiating dipole (p_z) of the tip, which is roughly proportional to the scattering field E_s measured by the s-SNOM [9,44]. Due to the elongated shape of the tip, we neglect horizontal dipole moments of the tip (p_x and p_y) that are orders of magnitude weaker than p_z. Note that the s-SNOM is commonly built based on a tapping-mode atomic force microscope (AFM). The tapping amplitude (A) is typically in the order of tens of nanometers (A set to be 40 nm in the current work). As a result, the scattering signal is naturally modulated due to the tapping of the tip. Demodulation of the scattering signal at n^{th} harmonics ($n \geq 2$) of the tapping frequency can significantly suppress the background signals and thus capturing genuine near-field responses [43,44,46]. In our modeling, we mimic the modulation & demodulation data acquisition process of s-SNOM, and obtain the n^{th} harmonics of the near-field amplitude signal ($n = 3$ in the current work) by calculating p_z of the tip at multiple tip-sample separations [45]. For the purpose of quantitative comparison, we normalized the s-SNOM amplitude signal to that of silicon due to the flat spectral response of silicon in the mid-IR region. In all the calculated nano-IR spectra shown below, we plot the normalized near-field amplitude signal (s) of s-SNOM. The signal to noise ratio of an optimally-aligned s-SNOM is up to ~100 when measuring silicon, so any spectroscopic features with sizes larger than ~1% of the signal of silicon could be observable in practical s-SNOM experiments with optimized alignment.

Graphene is modeled as a 3D metal with a thickness of $t_g = 0.34$ nm, and the corresponding 3D optical conductivity is set to be $\sigma_{3D} = \sigma_{2D}/t_g$, where the 2D conductivity of graphene (σ_{2D}) is obtained with the random-phase approximation method as detailed in Ref. [9]. The two parameters of graphene are the Fermi energy (E_F) and the phenomenological scattering rate γ. The latter is defined as the ratio between the charge scattering energy of graphene and the IR excitation energy. Throughout the main text, we set γ to be 0.1 that is consistent with previous experimental studies [9,10]. As a test, we show in Fig. S1 the near-field spectra of SiO_2 and graphene on SiO_2. The quantitative consistency between the modeling

results with previous experimental data [9,43] justifies the validity of our model. Detailed discussions about the test modeling results are given in the Supplemental Material [45].

B. Breathing-mode plasmon resonances.

With the quantitative model, we first study the spectroscopic responses of GNDs on a CaF_2 substrate. The optical constants of CaF_2 that we used in the modeling are adoped from previous literature [47]. As shown in Fig. S2, CaF_2 has a relatively flat mid-IR response in a wide spectral range above 60 meV. The spectral response below 60 meV is dominated by optical phonons of CaF_2. As a comparison, the commonly-used SiO_2 substrate has three optical resonances centered at around 50 meV, 100 meV, and 140 meV, respectively (Fig. S2). Therefore, CaF_2 serves as a better substrate compared to SiO_2 for revealing the pure plasmonic responses of graphene in the wide mid-IR region, as confirmed by previous experimental studies [21,25].

Figure 2(a) presents the calculated nano-IR spectra of GNDs with various radius (r) using our s-SNOM model. For all the calculations, the tip is located at the center of the GNDs. The E_F of graphene is set to be 0.2 eV. The key features in the calculated s-SNOM spectra are the resonance peaks (marked with arrows). The number of resonance peaks within the considered spectral region (60 – 160 meV) increases with the GND radius. As shown in the top panel of Fig. 2(a), there is clearly one dominant peak (marked with the black arrow) in the near-field spectrum of the GND with r = 50 nm. As r increases, the dominant peak (black arrow) shifts to lower energies and the 2nd (blue arrow) and 3rd (red arrow) peaks emerge at higher energies. More peaks emerge in even larger GNDs (e.g. r = 300 - 500 nm). Nevertheless, the higher-order peaks are much weaker and closer to each other, so they become less distinguishable. They can be seen more clearly in cleaner samples with a lower scattering rate (see Fig. S5 in the Supplemental Material [45]). Note that we used a logarithmic scale for the normalized IR amplitude in Fig. 2.

In addition to the size dependence, we also explored the doping dependence of these resonance modes. In Fig. 2(b), we plot the calculated nano-IR spectra of a 300-nm-radius GND with various E_F. Multiple resonance peaks (marked with arrows) are clearly seen in the spectra with $E_F \geq 0.1$ eV and the peak locations shift to higher energies as E_F increases. In the case of $E_F = 0.05$ eV [top panel of Fig. 2(b)], all the resonance peaks are close to or below 60 meV, so they are not fully shown in the field of view. Instead, the dominant feature here is originated from the interband transitions with onset energy at $2E_F$ (marked with vertical dashed line) [48-50].

The resonance modes of GNDs shown in Fig. 2 are originated from the BM plasmonic resonances. To demonstrate that, we computed the z-component electrical field (E_z) maps of GNDs at the first (black arrow), second (blue arrow) and third (red arrow) resonance locations of the GND with r = 300 nm and $E_F = 0.3$ eV [see Fig. 2(b)]. The corresponding out-of-plane (x-z plane, left panels) and in-plane (x-y plane, right panels) E_z maps are shown in Fig. 3, where one can see that the spatial field patterns correspond to BMs with different orders (n = 0, 1, 2 …). The order index assignment will be discussed in detail below. To verify the plasmonic origin of these BMs, we plot in Fig. 4(a) and Fig. 4(b) the resonant peak energies (E_p, data points) versus 1/r and E_F respectively based on the nano-IR spectra in Fig. 2. In both cases, E_p increase with increasing 1/r or E_F for all three resonance modes marked with arrows. Such dependence behaviors are fully consistent with the dispersion properties of graphene plasmons.

Under long-wavelength approximation, the dispersion relation of graphene plasmons is described by

$$q_p \approx \frac{i\varepsilon_0(1+\varepsilon_s)e}{\hbar}\frac{E}{\sigma_{2D}}, \quad [1]$$

where q_p is the plasmon wavevector, ε_s is the dielectric function of the CaF_2 substrate [45]. Under Drude approximation, the 2D conductivity of graphene can be written as

$$\sigma_{2D} \approx \frac{ie^2}{\pi\hbar}\frac{E_F}{E(1+i\gamma)}. \quad [2]$$

Based on Eq. (1) and Eq. (2), we have the plasmon energy

$$E_p^2 \approx \frac{e}{\pi\varepsilon_0(1+\varepsilon_s)}\sqrt{q_p E_F}. \quad [3]$$

Therefore, in a relatively flat dielectric environment, E_p scales with the square root of q_p and E_F. Similar to the DM plasmon resonance modes of GNRs, the characteristic mode wavevector q_p of a breathing mode in GNDs is also determined by the size of the disk. The mode equation can be written as:

$$q_p r + \Phi_R = n\pi , \quad [4]$$

where $\Phi_R \approx -0.75\pi$ is the anomalous phase shift upon reflection off the edge of graphene [12,51,52]. Equation 4 indicates that q_p is proportional to $1/r$ for all the resonance modes. Therefore, the $1/r$ and E_F dependence relations of plasmon resonance energy shown in Fig. 4 can be fully understood by Eq. (3) and Eq. (4). For the purpose of quantitative comparison, we plot in Fig. 4 calculated $1/r$ and E_F dependence relations (curves) of graphene plasmons based on Eq. (3) and Eq. (4). From Fig. 4, one can see that the resonance energies (data points) extracted from nano-IR spectra (Fig. 2) are generally consistent with the analytical curves, indicating that the observed resonance modes are indeed due to graphene plasmons. There are slight deviations (5-10%) in the $n = 0$ mode in Fig. 4(b) in small GNDs ($r = 50$ and 100 nm). This is mainly due to the impact of the metallic tip on the plasmon resonance energy of GND, which will have notable effects when the size of GND is very small. Similar phenomena have been observed experimentally in previous studies [53,54], where the strong coupling between graphene and adjacent metal layer leads to the formation of acoustic plasmons. More discussions about the tip-induced modification of plasmon resonance energy are given in the Supplemental Material [45].

C. Tip- and plasmon-enhanced vibrational modes of molecules.

Now we wish to study the enhancement effects of molecular vibrational modes by the tip-excited BM plasmonic resonances. We consider a disk-shaped particle consisting of pentacene molecules sitting at the center of the GND [see Fig. 1(a)]. Here the pentacene molecules are standing upright, which is energetically favored according to previous literature [55]. The thickness of the molecular disk is set to be ~1.6 nm which is roughly the length of the pentacene molecule. Other particle shapes are discussed in the Supplemental Material [45]. In our model, we use the vibrational mode of pentacene at 112 meV as an example. The enhancement effects on other vibrational modes of pentacene or other types of molecules are qualitatively similar. The vibrational mode is modeled by the following LT oscillator:

$$\varepsilon(E) = \varepsilon_\infty + \frac{SE_{TO}^2}{E_{TO}^2 - E^2 - iEE_\Gamma}, \quad [7]$$

where $\varepsilon_\infty = 2.981$, $E_{TO} \approx 112$ meV, $S = 0.0102$, and $E_\Gamma = 0.43$ meV according to Ref. [56].

The modeling results are shown in Fig. 5(a), where we plot the calculated nano-IR spectra of a molecular particle on GND (red curve), bare GND (black curve), and the bare molecular particle (blue curve). The radius of the molecular disk (ρ) is set to be 5 nm. The radius and Fermi energy of GND are set to be 100 nm and 0.26 eV, respectively. Under these settings, one can see a strong and broad resonance peak centered at 107 meV in the spectrum of bare GND [black curve in Fig. 5(a)], which is attributed to the $n = 0$ BM plasmon resonance. The bare molecule spectrum [blue curve in Fig. 5(a)], on the other hand, is extremely weak and is not seen on the same scale. A zoom-in view [inset of Fig. 5(a)] of the bare molecule spectrum shows the peak feature due to the molecule vibrational mode at about 112 meV. Nevertheless, the peak feature is only less than 0.001 when normalized to silicon [we multiply the amplitude signal by 150 times in the inset of Fig. 5(a)], so it is impossible for observation in practical measurements. Adding the GND underneath molecules significantly enhances the vibrational mode feature, which appears to be a sharp dip on top of the broad plasmon resonance. The dip feature has a size of 0.3 when normalized to silicon, so it can be easily detectable by s-SNOM. The formation of the dip feature instead of the peak feature is originated from the interference between the molecular vibrational mode with the plasmon resonance mode, which was described as the so-called "plasmon-induced transparency" in previous far-field studies [57,58]. From Fig. 5(a), we also notice variations of the plasmon resonance energy when comparing the spectrum of molecules/GND (red curve) to that of bare

GND (black curve). This is mainly due to the enlarged tip-GND separation after adding the molecular particle (see Supplemental Material [45]). Indeed, if intentionally increasing the tip-GND separation by 1.6 nm (the height of molecules), the plasmon resonance energy of bare GND [black dashed curve in Fig. 5(a)] matches better that of molecules on GND [red curve in Fig. 5(a)].

Now we wish to explore the sensitivity limit of the proposed method for probing extremely small molecular particles. As shown in Fig. 5(b), we plot the calculated s-SNOM spectra of molecular disks with various radii (ρ) on GNDs. Clearly, the dip feature due to the vibrational mode can be visualized in molecules with a disk radius down to 1 nm, corresponding to a volume of about 5 nm^3. The relative size of the dip feature is close to 0.05 when normalized to silicon, so it is clearly detectable by s-SNOM. Such a high sensitivity is impossible with traditional diffraction-limited IR spectroscopy or nano-FTIR without GND. The highest sensitivity demonstrated so far with s-SNOM alone is reported in Ref. [59], where the vibrational modes of biomolecules with a volume ~ 900 nm^3 (sphere with a diameter of 12 nm) were observed. Therefore, with additional enhancement by the BM plasmon resonance of GND, the probing sensitivity increases dramatically.

The capability of ultra-sensitive detection is originated from the strong field enhancement from both the metal tip and the BM plasmon resonance of GND. To demonstrate that, in Fig. 6, we compare the simulated E_z field maps with four different settings: (1) metal tip with GND [Fig. 6(a)], (2) silicon tip with GND [Fig. 6(b)], (3) metal tip without GND [Fig. 6(c)], and (4) silicon tip without GND [Fig. 6(d)]. As a general example, we set the tip-sample distance to be 5 nm, the excitation energy to be 112 meV that matches the resonance energy of GND with E_F = 0.26 eV. The metal here is set to be platinum that is commonly used for the coating material of s-SNOM tips. The purpose of comparing the metal tip with a silicon tip is to evaluate the field enhancement effects due to the metallic tip of s-SNOM (the field enhancement effects due to a silicon tip is limited). From the simulations (Fig. 6), we find that the metal tip with GND [Fig. 6(a)] produces the highest field amplitude ($|E_z|$) underneath the tip, which is ~5 times higher than that with a silicon tip and GND [Fig. 6(b)], ~10 times higher than that with metal tip but no GND [Fig. 6(c)], ~24 times higher than that with bare silicon tip [Fig. 6(d)], and ~225 times compared to that of the far-field excitation field. Therefore, the strong field enhancement is originated from both the metallic tip and the BM plasmon resonance of GND. Note that the E_z field values here are mainly for a qualitative understanding of the enhancement effects. To understand the exact size or shape of the spectroscopic feature of the vibrational mode in Fig. 5, one needs to consider the interference between the molecule vibrational mode and plasmon resonance mode of GND as well as the complicated tip modulation & demodulation signal acquisition processes.

Finally, we wish to discuss several considerations related to practical applications of the proposed method. First, the plasmon enhancement effect described above requires matching between the plasmon resonance energy with the vibrational mode of molecules. Nevertheless, the match is not stringent due to the broad resonance of the n = 0 BM plasmon resonance of GND. As shown in Fig. 5(c,d), we plot the calculated nano-IR spectra with variations of E_F [0.22 – 0.30 eV, see Fig. 5(c)] and the GND radius [80-110 nm, see Fig. 5(d)]. The spectroscopic feature due to the molecule vibrational mode can be seen clearly in all the spectra indicating that the requirements of selecting E_F or GND radius for experimental measurements are not stringent. Second, all the modeling results discussed above assume that the tip and molecule are right at the center of GND. In fact, even the tip and molecules are slightly off the center, field enhancement effects due to both the tip and GND are still strong. For example, when the tip is 20 nm and 40 nm away from the center of GND with r = 100 nm, the E_z field amplitude only drops by 12% and 35%, respectively (Fig. S6). Third, for practical experiments, we propose to fabricate electrically-connected GND arrays with chemical-vapor-deposited graphene (Fig. S7, similar to the device shown in Ref. [60]). Such devices are economically feasible for fabrications based on common lithography methods. These densely distributed GND arrays act as a testbed, where molecules or other nanoparticles of interest can be dispersed on top. After locating the molecular particle on GNDs with AFM topography scanning, one can perform nano-FTIR spectroscopy after optimizing the signals of the molecular vibrational modes with electrical gating.

III. CONCLUSION

In conclusion, we demonstrate through vigorous modeling a novel method for ultra-sensitive IR vibrational spectroscopy by taking advantage of the field enhancement of both a sharp metallic tip and the BM plasmon resonances of GNDs. Due to the two-fold enhancement, the electric field between the tip apex and the GND can be orders of magnitude higher than that of the free-space excitation field. As a result, an ultra-high sensitivity to molecular vibrational modes could be achieved, which enables the detection of molecular particles with a size down to 1-2 nm. Note that the field enhancement method proposed here is not only suitable for probing IR vibrational modes of molecules or phonon modes of crystalline nanoparticles, it can also be used to probe high-field nonlinear effects [61] of nanoparticles in the mid-IR region. Our work paves the way for practical applications of tip- and plasmon-enhanced IR spectroscopy for ultra-sensitive detections and characterizations of small molecules and nanoparticles.

ACKNOWLEDGMENTS

Work done at Ames Lab was supported by the U.S. Department of Energy, Office of Basic Energy Science, Division of Materials Sciences and Engineering. Ames Laboratory is operated for the U.S. Department of Energy by Iowa State University under Contract No. DE-AC02-07CH11358.

REFERENCES

1. V. Ryzhii, A. Satou, and T. Otsuji, Plasma Waves in Two-Dimensional Electron-Hole System in Gated Graphene Heterostructures, J. Appl. Phys. **101**, 024509 (2007).
2. M. Jablan, H. Buljan, and M. Soljačić, Plasmonics in Graphene at Infrared Frequencies, Phys. Rev. B **80**, 245435 (2009).
3. F. H. L. Koppens, D. E. Chang, and F. Javier García de Abajo, Graphene Plasmonics: A Platform for Strong Light-Matter Interactions, Nano Lett. **11**, 3370-3377 (2011).
4. A. N. Grigorenko, M. Polini, and K. S. Novoselov, Graphene Plasmonics, Nat. Photon. **6**, 749 (2012).
5. T. Low and P. Avouris, Graphene Plasmonics for Terahertz to Mid-Infrared Applications, ACS Nano **8**, 1086 (2014).
6. D. N. Basov, M. M. Fogler, and F. J. García de Abajo, Polaritons in van der Waals Materials, Science **354**, 195-195 (2016).
7. T. Low, A. Chaves, J. D. Caldwell, A. Kumar, N. X. Fang, P. Avouris, T. F. Heinz, F. Guinea, L. Martin-Moreno, and F. Koppens, Polaritons in Layered Two-Dimensional Materials, Nat. Mater. **16**, 182–194 (2017).
8. L. Ju, B. Geng, J. Horng, C. Girit, M. Martin, Z. Hao, H. A. Bechtel, X. Liang, A. Zettl, Y. R. Shen, and F. Wang, Graphene Plasmonics for Tunable Terahertz Metamaterials, Nat. Nanotechnol. **6**, 630-634 (2011).
9. Z. Fei, G. O. Andreev, W. Bao, L. M. Zhang, A. S. McLeod, C. Wang, M. K. Stewart, Z. Zhao, G. Dominguez, M. Thiemens, M. M. Fogler, M. J. Tauber, A. H. Castro-Neto, C. N. Lau, F. Keilmann, and D. N. Basov, Infrared Nanoscopy of Dirac Plasmons at the Graphene–SiO_2 Interface, Nano Lett. **11**, 4701-4705 (2011).
10. Z. Fei, A. S. Rodin, G. O. Andreev, W. Bao, A. S. McLeod, M. Wagner, L. M. Zhang, Z. Zhao, M. Thiemens, G. Dominguez, M. M. Fogler, A. H. Castro Neto, C. N. Lau, F. Keilmann, and D. N. Basov, Gate-Tuning of Graphene Plasmons Revealed by Infrared Nano-Imaging, Nature **487**, 82-85 (2012).
11. J. Chen, M. Badioli, P. Alonso-González, S. Thongrattanasiri, F. Huth, J. Osmond, M. Spasenović, A. Centeno, A. Pesquera, P. Godignon, A. Z. Elorza, N. Camara, F. J. García de Abajo, R. Hillenbrand, and F. H. L. Koppens, Optical Nano-Imaging of Gate-Tunable Graphene Plasmons, Nature **487**, 77-81 (2012).
12. V. W. Brar, M. S. Jang, M. Sherrott, J. J. Lopez, and H. Atwater, Highly Confined Tunable Mid-Infrared Plasmonics in Graphene Nanoresonators, Nano Lett. **13**, 2541-2547 (2013).

13. Z. Fang, S. Thongrattanasiri, A. Schlather, Z. Liu, L. Ma, Y. Wang, P. Ajayan, P. Nordlander, N. J. Halas, and F. J. G. de Abajo, Gated Tunability and Hybridization of Localized Plasmons in Nanostructured Graphene, ACS Nano **7**, 2388-2395 (2013).
14. W. Gao, G. Shi, Z. Jin, J. Shu, Q. Zhang, R. Vajtai, P. M. Ajayan, J. Kono, and Q. Xu, Excitation and Active Control of Propagating Surface Plasmon Polaritons in Graphene, Nano Lett. **13**, 3698-3702 (2013).
15. Z. Fei, J. J. Foley IV, W. Gannett, M. K. Liu, S. Dai, G. X. Ni, A. Zettl, M. M. Fogler, G. P. Wiederrecht, S. K. Gray, and D. N. Basov, Ultraconfined plasmonic hotspots inside graphene nanobubbles, Nano Lett. **16**, 7842-7848 (2016).
16. F. Hu, Y. Luan, Z. Fei, I. Z. Palubski, M. D. Goldflam, S. Dai, J. S. Wu, K. W. Post, G. C. A. M. Janssen, M. M. Fogler, and D. N. Basov, Imaging the localized plasmon resonance modes in graphene nanoribbons, Nano Lett. **17**, 5423-5428 (2017).
17. A. Woessner, M. B. Lundeberg, Y. Gao, A. Principi, P. Alonso-González, M. Carrega, K. Watanabe, T. Taniguchi, G. Vignale, M. Polini, J. Hone, R. Hillenbrand, and F. H. L. Koppens, Highly confined low-loss plasmons in graphene–boron nitride heterostructures, Nat. Mater. **14**, 421-425 (2015).
18. G. X. Ni, A. S. McLeod, Z. Sun, L. Wang, L. Xiong, K. W. Post, S. S. Sunku, B.-Y. Jiang, J. Hone, C. R. Dean, M. M. Fogler, and D. N. Basov, Fundamental limits to graphene plasmonics, Nature **557**, 530-533 (2018).
19. F. Hu, M. Kim, Y. Zhang, Y. Luan, K.-M. Ho, Y. Shi, C.-Z. Wang, X. Wang, and Z. Fei, Tailored Plasmons in Pentacene/Graphene Heterostructures with Interlayer Electron Transfer, Nano Lett. **19**, 6058-6064 (2019).
20. D. Rodrigo, O. Limaj, D. Janner, D. Etezadi, F. Javier García de Abajo, V. Pruneri, and H. Altug, Mid-infrared plasmonic biosensing with graphene, Science **349**, 165-168 (2015).
21. H. Hu, X. Yang, F. Zhai, D. Hu, R. Liu, K. Liu, Z. Sun, and Q. Dai, Far-field nanoscale infrared spectroscopy of vibrational fingerprints of molecules with graphene plasmons, Nat. Commun. **7**, 12334 (2016).
22. Y. Li, H. Yan, D. B. Farmer, X. Meng, W. Zhu, R. M. Osgood, T. F. Heinz, and P. Avouris, Graphene Plasmon Enhanced Vibrational Sensing of Surface Adsorbed Layers, Nano Lett. **14**, 1573-1577 (2014).
23. H. Hu, X. Yang, X. Guo, K. Khaliji, S. R. Biswas, F. Javier García de Abajo, T. Low, Z. Sun, and Q. Dai, Gas identification with graphene plasmons, Nat. Commun. **10**, 1131 (2019).
24. F.-P. Schmidt, H. Ditlbacher, U. Hohenester, A. Hohenau, F. Hofer, and J. R. Krenn, Dark Plasmonic Breathing Modes in Silver Nanodisks, Nano Lett. **12**, 5780-5783 (2012).
25. A. Y. Nikitin, P. Alonso-González, S. Vélez, S. Mastel, A. Centeno, A. Pesquera, A. Zurutuza, F. Casanova, L. E. Hueso, F. H. L. Koppens, and R. Hillenbrand, Real-space mapping of tailored sheet and edge plasmons in graphene nanoresonators, Nat. Photon **10**, 239-243 (2016).
26. S. Chen, M. Autore, J. Li, P. Li, P. Alonso-Gonzalez, Z. Yang, L. Martin-Moreno, R. Hillenbrand, and A. Y. Nikitin, Acoustic Graphene Plasmon Nanoresonators for Field-Enhanced Infrared Molecular Spectroscopy, ACS Photonics **4**, 3089-3097 (2017).
27. S. Dai, Z. Fei, Q. Ma, A. S. Rodin, M. Wagner, A. S. McLeod, M. K. Liu, W. Gannett, W. Regan, K. Watanabe, T. Taniguchi, M. Thiemens, G. Dominguez, A. H. Castro Neto, A. Zettl, F. Keilmann, P. Jarillo-Herrero, M. M. Fogler, and D. N. Basov, Tunable Phonon Polaritons in Atomically Thin van der Waals Crystals of Boron Nitride, Science **343**, 1125-1129 (2014).
28. J. D. Caldwell, A. V. Kretinin, Y. Chen, V. Giannini, M. M. Fogler, Y. Francescato, C. T. Ellis, J. G. Tischler, C. R. Woods, A. J. Giles, M. Hong, K. Watanabe, T. Taniguchi, S. A. Maier, K. S. Novoselov, Sub-diffractional volume-confined polaritons in the natural hyperbolic material hexagonal boron nitride, Nat. Commun. **5**, 5221 (2014).
29. Z. Shi, H. A. Bechtel, S. Berweger, Y. Sun, B. Zeng, C. Jin, H. Chang, M. C. Martin, M. B. Raschke, and F. Wang, Amplitude- and Phase-Resolved Nanospectral Imaging of Phonon Polaritons in Hexagonal Boron Nitride, ACS Photonics **2**, 790-796 (2015).

30. E. Yoxall, M. Schnell, A. Y. Nikitin, O. Txoperena, A. Woessner, M. B. Lundeberg, F. Casanova, L. E. Hueso, F. H. L. Koppens, and R. Hillenbrand, Direct observation of ultraslow hyperbolic polariton propagation with negative phase velocity, Nat. Photon. **9**, 674-678 (2015).
31. Z. Zheng, J. Chen, Y. Wang, X. Wang, X. Chen, P. Liu, J. Xu, W. Xie, H. Chen, S. Deng, and N. Xu, Highly Confined and Tunable Hyperbolic Phonon Polaritons in Van Der Van Der Waals Semiconducting Transition Metal Oxides, Adv. Mater. **30**, 1705318 (2018).
32. W. Ma, P. Alonso-González, S. Li, A. Y. Nikitin, J. Yuan, J. Martín-Sánchez, J. Taboada-Gutiérrez, I. Amenabar, P. Li, S. Vélez, C. Tollan, Z. Dai, Y. Zhang, S. Sriram, K. Kalantar-Zadeh, S.-T. Lee, R. Hillenbrand, and Q. Bao, In-plane anisotropic and ultra-low-loss polaritons in a natural van der Waals crystal, *Nature* **2018**, 562, 557-562.
33. F. Hu, Y. Luan, M. E. Scott, J. Yan, D. G. Mandrus, X. Xu, and Z. Fei, Imaging exciton–polariton transport in $MoSe_2$ waveguides, Nat. Photonics **11**, 356-360 (2017).
34. M. Mrejen, L. Yadgarov, A. Levanon, and H. Suchowski, Transient exciton-polariton dynamics in WSe_2 by ultrafast near-field imaging, Sci. Adv. **5**, eaat9618 (2019).
35. F. Hu, Y. Luan, J. Speltz, D. Zhong, C. H. Liu, J. Yan, D. G. Mandrus, X. Xu, and Z. Fei, Imaging propagative exciton polaritons in atomically thin WSe_2 waveguides, Phys. Rev. B **100**, 121301 (2019).
36. F. Hu and Z. Fei, Recent Progress on Exciton Polaritons in Layered Transition-Metal Dichalcogenides, Adv. Opt. Mater. **2019**, 1901003 (2019).
37. I. Amenabar, S. Poly, W. Nuansing, E. H. Hubrich, A. A. Govyadinov, F. Huth, R. Krutokhvostov, L. Zhang, M. Knez, J. Heberley, A. M. Bittner, and R. Hillenbrand, Structural analysis and mapping of individual protein complexes by infrared Nanospectroscopy, Nat. Commun. **4**, 2890 (2013).
38. F. Huth, A. Govyadinov, S. Amarie, W. Nuansing, F. Keilmann, and R. Hillenbrand, Nano-FTIR Absorption Spectroscopy of Molecular Fingerprints at 20 nm Spatial Resolution, Nano Lett. **12**, 3973-3978 (2012).
39. C. Westermeier, A. Cernescu, S. Amarie, C. Liewald, F. Keilmann, and B. Nickel, Sub-micron phase coexistence in small-molecule organic thin films revealed by infrared nano-imaging, Nat. Commun. **5**, 4101 (2014).
40. B. Pollard, E. A. Muller, K. Hinrichs, and M. B. Raschke, Vibrational nano-spectroscopic imaging correlating structure with intermolecular coupling and dynamics, Nat. Commun. **5**, 3587 (2014).
41. A. Cvitkovic, N. Ocelic, and R. Hillenbrand, Analytical model for quantitative prediction of material contrasts in scattering-type near-field optical microscopy, Opt. Express **15**, 8550-8565 (2007).
42. B. Hauer, A. P. Engelhardt, and T. Taubner, Quasi-analytical model for scattering infrared near-field microscopy on layered systems, Opt. Express **20**, 13173-13188 (2012).
43. L. M. Zhang, G. O. Andreev, Z. Fei, A. S. McLeod, G. Dominguez, M. Thiemens, A. H. Castro-Neto, D. N. Basov, and M. M. Fogler, Near-field spectroscopy of silicon dioxide thin films, Phys. Rev. B **85**, 075419 (2012).
44. A. S. McLeod, P. Kelly, M. D. Goldflam, Z. Gainsforth, A. J. Westphal, G. Dominguez, M. H. Thiemens, M. M. Fogler, and D. N. Basov, model for quantitative tip-enhanced spectroscopy and the extraction of nanoscale-resolved optical constants, Phys. Rev B **90**, 085136 (2014).
45. See Supplemental Material for more introductions about modeling methods and results.
46. B. Knoll and F. Keilmann, Enhanced dielectric contrast in scattering-type scanning near-field optical microscopy, Opt. Commun. **182**, 321-328 (2000).
47. W. Kaiser, W. G. Spitzer, R. H. Kaiser, and L. E. Howarth, Infrared Properties of CaF_2, SrF_2, and BaF_2, *Phys. Rev*. **127**, 1950-1954 (1950)**.**
48. Z. Q. Li, E. A. Henriksen, Z. Jiang, Z. Hao, M. C. Martin, P. Kim, H. L. Stormer, and D. N. Basov, Dirac charge dynamics in graphene by infrared spectroscopy, Nat. Phys. **4**, 532-535 (2008).
49. F. Wang, Y. Zhang, C. Tian, C. Girit, A. Zettl, M. Crommie, and Y. R. Shen, Gate-variable optical transitions in graphene, Science **320**, 206-209 (2008).
50. K. F. Mak, M. Y. Sfeir, Y. Wu, C. H. Lui, J. A. Misewich, and T. F. Heinz, Measurement of the optical conductivity of graphene, Phys. Rev. Lett. **101**, 196405 (2008).

51. K. A. Velizhanin, Geometric universality of plasmon modes in graphene nanoribbon arrays, Phys. Rev. B **91**, 125429 (2015).
52. A. Y. Nikitin, T. Low, and L. Martin-Moreno, Anomalous reflection phase of graphene plasmons and its influence on resonators, Phys. Rev. B **90**, 041407(R) (2014).
53. P. Alonso-González, A. Y. Nikitin, Y. Gao, A. Woessner, M. B. Lundeberg, A. Principi, N. Forcellini, W. Yan, S. Vélez, A. J. Huber, K. Watanabe, T. Taniguchi, F. Casanova, L. E. Hueso, M. Polini, J. Hone, F. H. L. Koppens, and R. Hillenbrand, Acoustic terahertz graphene plasmons revealed by photocurrent nanoscopy, Nat. Nanotechnol. **12**, 31-35 (2017).
54. L.-H. Lee, D. Yoo, P. Avouris, T. Low, and S.-H. Oh, Graphene acoustic plasmon resonator for ultrasensitive infrared spectroscopy, Nat. Nanotechnol. **14**, 313-319 (2019).
55. A. O. F. Jones, B. Chattopadhyay, Y. H. Geerts, and R. Resel, Substrate-Induced and Thin-Film Phases: Polymorphism of Organic Materials on Surfaces, Adv. Funct. Mater. **26**, 2233-2255 (2016).
56. M. Schubert and C. Bundesmann, Infrared dielectric function and vibrational modes of pentacene thin films, Appl. Phys. Lett. **84**, 200 (2004).
57. H. Yan, T. Low, F. Guinea, F. Xia, and P. Avouris, Tunable Phonon-Induced Transparency in Bilayer Graphene Nanoribbons, Nano Lett. **14**, 4581-4586 (2014).
58. D. B. Farmer, P. Avouris, Y. Li, T. F. Heinz, and S.-J. Han, Ultrasensitive Plasmonic Detection of Molecules with Graphene, ACS Photonics **3**, 553-557 (2016).
59. I. Amenabar, S. Poly, W. Nuansing, E. H. Hubrich, A. A. Govyadinov, F. Huth, R. Krutokhvostov, L. Zhang, M. Knez, J. Heberle, A. M. Bittner, and R. Hillenbrand, Structural analysis and mapping of individual protein complexes by infrared Nanospectroscopy, Nat. Commun. **4**, 2890 (2013).
60. Q. Guo, R. Wu, C. Li, S. Yuan, B. Deng, F. Javier García de Abajo, and F. Xia, Efficient electrical detection of mid-infrared graphene plasmons at room temperature, Nat. Mater. **17**, 986-992 (2018).
61. I. Razdolski, Y. Chen, A. J. Giles, S. Gewinner, W. Schöllkopf, M. Hong, M. Wolf, V. Giannini, J. S. Caldwell, S. A. Maier, and A. Paarmann, Resonant Enhancement of Second-Harmonic Generation in the Mid-Infrared Using Localized Surface Phonon Polaritons in Subdiffractional Nanostructures, Nano Lett. **16**, 6954-6959 (2016).

Figure captions

Fig. 1. (a), Illustration of the quantitative model of s-SNOM on a molecule/GND sample. The GND has a radius of r. The molecular particle has a disk shape with a radius of ρ and thickness of h. The s-SNOM tip is approximated as a spheroid with a length of L and a tip-apex radius of a. (b) Modeled E_z field map at the x-z plane revealing tip-excited plasmonic breathing mode (BM) of a GND. Inset plots the in-plane (x-y plane) E_z field map revealing the plasmonic BM with a circular symmetry.

Fig. 2. (a) Modeled nano-IR spectra of GNDs with various disk radii on a CaF_2 substrate. The Fermi energy (E_F) of graphene is set to be 0.2 eV. (b) Calculated nano-IR spectra of GNDs on a CaF_2 substrate with varying E_F. The GND radius (r) is set to be 300 nm. The vertical dashed line in the top panel of (b) marks the onset of interband transitions at $E = 2E_F$. In all panels, a logarithmic scale is used in the y-axis to better visualize all resonance peaks, and the IR amplitude is normalized to that of a bare silicon substrate.

Fig. 3. Modeled E_z field maps of the n = 0, 1, 2 [from (a) to (c)] BM plasmons of the GND with r = 300 nm and E_F = 0.3 eV. The resonance energies (E_p) of the n = 0, 1, 2 modes are about 77 meV, 109 meV, and 133 meV, respectively [see Fig. 2(b)]. The left and right panels are for x-z and x-y planes, respectively. The field patterns of BM plasmons in GNDs with other radius and Fermi energies share similar characteristics.

Fig. 4. (a) Dependence relationship of the resonance energy E_p on E_F for the n = 0, 1, 2 resonance modes. (b) Dependence relationship of E_p on $1/r$ for the n = 0, 1, 2 resonance modes. Data points are extracted

from the modeled nano-IR spectra in Fig. 2. The color curves were calculated with analytical equations [Eq. (3) and Eq. (4)].

Fig. 5. (a) Modeled nano-IR spectra of bare GND (black curve), bare molecules (blue curve), and molecules on GND (red curve). The black dashed curve is for the spectrum of bare GND when the tip-sample distance increases by 1.6 nm (thickness of molecular disk). Inset plots a zoom-in view (amplitude × 150) of the spectrum of bare molecules. Here, Fermi energy is E_F = 0.26 eV, GND radius is r = 100 nm, and molecule disk radius is ρ = 5 nm. (b) Modeled nano-IR spectra of a molecular disk on GND with various molecule disk radii. Here, E_F = 0.26 eV and r = 100 nm. (c) Modeled nano-IR spectra of molecules with various E_F of GND. Here, r = 100 nm and ρ = 5 nm. (d) Modeled nano-IR spectra of molecules on GND with various radii of GND. Here, E_F = 0.26 and ρ = 5 nm. In all panels, the IR amplitude is normalized to that of a bare silicon substrate.

Fig. 6. Modeled E_z field maps of the tip-sample system with 4 different settings: (a) metal tip with GND, (b) silicon tip with GND, (c) metal tip without GND, and (d) silicon tip without GND.

Figure 1

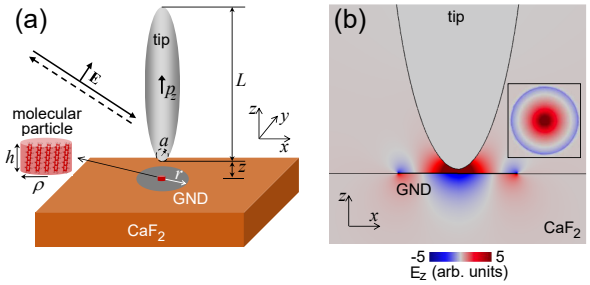
(a)
tip
E
p_z
L
molecular particle
h
ρ
a
r
z
GND
CaF2
z
y
x
(b)
tip
GND
CaF2
z
x
-5
5
Ez (arb. units)

Figure 2

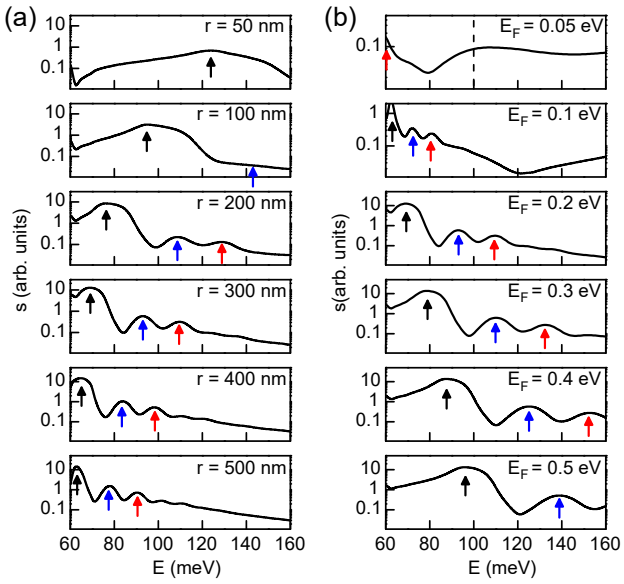
(a)
(b)
r = 50 nm
r = 100 nm
r = 200 nm
r = 300 nm
r = 400 nm
r = 500 nm
E_F = 0.05 eV
E_F = 0.1 eV
E_F = 0.2 eV
E_F = 0.3 eV
E_F = 0.4 eV
E_F = 0.5 eV
s (arb. units)
s(arb. units)
E (meV)
E (meV)
10
1
0.1
60
80
100
120
140
160

Figure 3

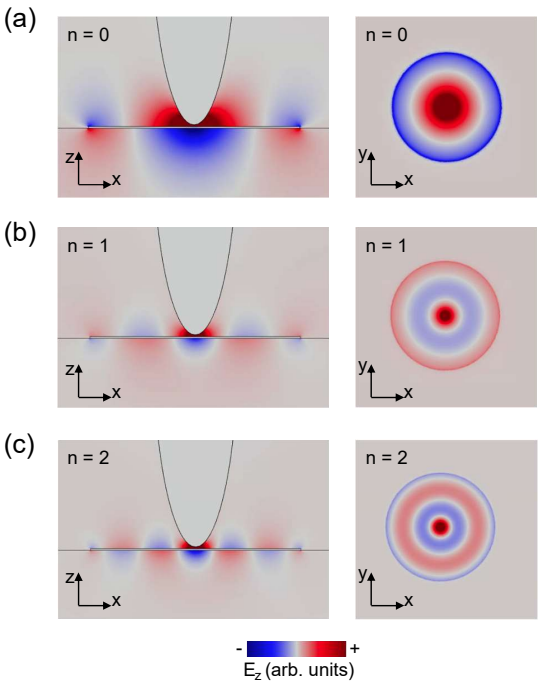

Figure 4

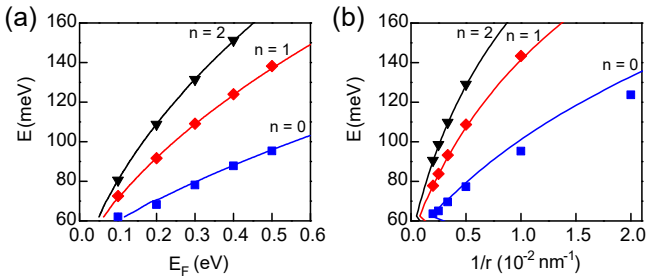
(a)
E (meV)
160
140
120
100
80
60
n = 2
n = 1
n = 0
0.0 0.1 0.2 0.3 0.4 0.5 0.6
E_F (eV)
(b)
E (meV)
160
140
120
100
80
60
n = 2
n = 1
n = 0
0.0 0.5 1.0 1.5 2.0
1/r (10^{-2} nm^{-1})

Figure 5

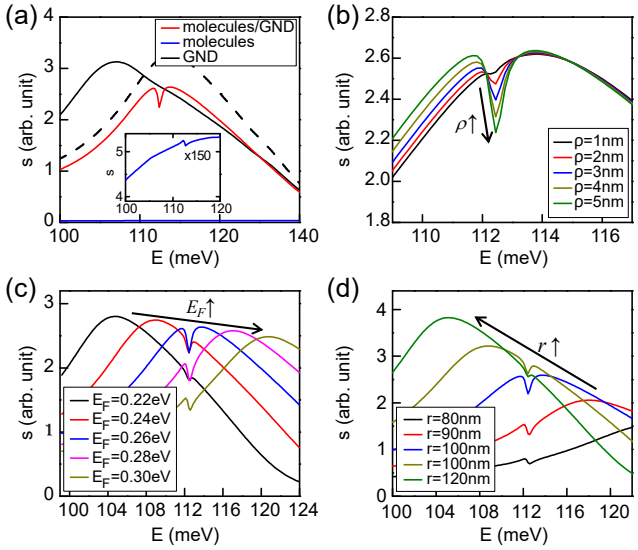
(a)
molecules/GND
molecules
GND
x150
s (arb. unit)
E (meV)
(b)
ρ↑
ρ=1nm
ρ=2nm
ρ=3nm
ρ=4nm
ρ=5nm
s (arb. unit)
E (meV)
(c)
E_F↑
E_F=0.22eV
E_F=0.24eV
E_F=0.26eV
E_F=0.28eV
E_F=0.30eV
s (arb. unit)
E (meV)
(d)
r↑
r=80nm
r=90nm
r=100nm
r=100nm
r=120nm
s (arb. unit)
E (meV)

Figure 6

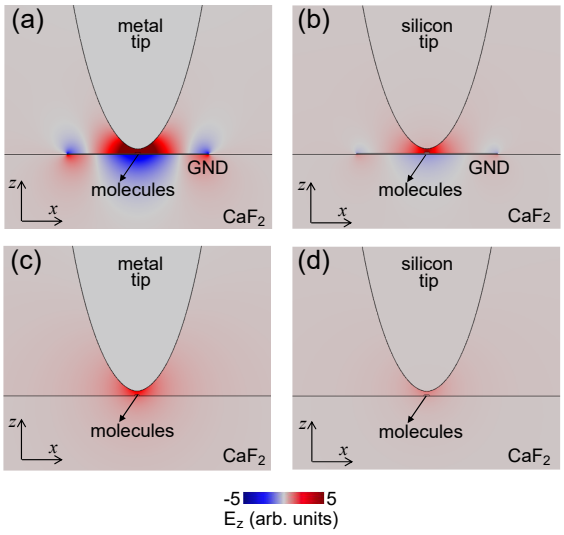
(a)
metal tip
GND
molecules
z
x
CaF2
(b)
silicon tip
GND
molecules
z
x
CaF2
(c)
metal tip
molecules
z
x
CaF2
(d)
silicon tip
molecules
z
x
CaF2
-5
5
Ez (arb. units)